COMPUTER RESEARCH AND MODELING
2026 VOL. 18 NO. 5 P. 1223–1247
DOI: 10.20537/2076-7633-2026-18-5-1223-1247

КиМ

MODELS IN PHYSICS AND TECHNOLOGY

UDC: 004.94:519.6:621.375.826:666.192

A surrogate modeling approach for laser polishing of quartz glass

L. N. Marchenko[1,a], Yu. V. Nikityuk[1,b], Iu. V. Bruttan[2,c], V. A. Prokhorenko[1,d], H. Zhang[3,e], A. Zhang[3,f], S. I. Sokolov[1,g]

[1]Francisk Skorina Gomel State University,
104 Sovetskaya st., Gomel, 246028, Belarus
[2]Pskov State University,
2 Lenin sq., Pskov, 180000, Russia
[3]Nanjing University of Science and Technology,
200 Xiaolingwei st., Nanjing, 210094, China

E-mail: [a] lmarchenko@gsu.by, [b] nikitjuk@gsu.by, [c] bruttan@mail.ru, [d] shnysct@gmail.com,
[e] hongchao@njust.edu.cn, [f] zhangaijun@njust.edu.cn, [g] sokolov@gsu.by

Received 20.09.2026, after completion — 09.10.2026.
Accepted for publication 10.10.2026.

The study addresses surrogate modeling of thermomechanical responses in quartz-glass laser polishing using finite-element simulation data. The relationships between thermal and mechanical responses and the main process parameters — laser power, source travel speed, and laser-spot radius — are investigated. Classical and regularized regression models, support-vector regression, tree-based ensembles, physics-structured models, tensor-product B-splines, and evolutionarily synthesized neural networks are compared using a common training, validation, and independent test split. Stacking ensembles based on Random Forest, Gradient Boosting, and XGBoost provided the lowest prediction errors for all investigated responses, with test coefficients of determination above 0.998. Physics-structured models were less accurate in terms of minimum prediction error but provided smooth and interpretable relationships between laser-processing parameters and thermomechanical responses. Evolutionary architecture search produced a two-output neural-network model for simultaneous prediction of the maximum temperature and maximum equivalent stress. Within the investigated dataset, source travel speed has the highest permutation importance for the predictive accuracy of the selected models. The results demonstrate that different classes of surrogate models are suitable for different modeling objectives: ensemble models are preferable when high predictive accuracy is required, physics-structured models are useful for response analysis and physical interpretation, and neural models provide simultaneous approximation of coupled thermal and mechanical responses. The developed surrogate models can therefore be used as a computationally efficient basis for analyzing laser-polishing regimes and for subsequent multicriteria optimization with simultaneous consideration of temperature and stress constraints.

Keywords: laser polishing, quartz glass, finite-element modeling, thermoviscoelasticity, surrogate model, physics-structured features, tensor B-splines, ensemble learning, neuroevolution

Citation: *Computer Research and Modeling*, 2026, vol. 18, no. 5, pp. 1223–1247.

© 2026 Larysa N. Marchenko, Yurii V. Nikityuk, Iuliia V. Bruttan, Vladislav A. Prokhorenko, Hongchao Zhang, Aijun Zhang, Sergey I. Sokolov
This work is licensed under the Creative Commons Attribution-NoDerivs 3.0 Unported License.
To view a copy of this license, visit http://creativecommons.org/licenses/by-nd/3.0/
or send a letter to Creative Commons, PO Box 1866, Mountain View, CA 94042, USA.

КОМПЬЮТЕРНЫЕ ИССЛЕДОВАНИЯ
И МОДЕЛИРОВАНИЕ 2026 Т. 18 № 5 С. 1223–1247
DOI: 10.20537/2076-7633-2026-18-5-1223-1247

Ки&М

МОДЕЛИ В ФИЗИКЕ И ТЕХНОЛОГИИ

УДК: 004.94:519.6:621.375.826:666.192

Суррогатное моделирование процессов лазерной полировки кварцевых стекол

Л. Н. Марченко[1,a], Ю. В. Никитюк[1,b], Ю. В. Бруттан[2,c], В. А. Прохоренко[1,d], Х. Чжан[3,e], А. Чжан[3,f], С. И. Соколов[1,g]

[1]Гомельский государственный университет имени Франциска Скорины,
Беларусь, 246028, г. Гомель, ул. Советская, д. 104
[2]Псковский государственный университет,
Россия, 180000, г. Псков, пл. Ленина, д. 2
[3]Нанкинский университет науки и технологий,
Китайская Народная Республика, 210094, г. Нанкин, провинция Цзянсу, район Сюаньу, ул. Сяолинвэй, д. 200

E-mail: [a] lmarchenko@gsu.by, [b] nikitjuk@gsu.by, [c] bruttan@mail.ru, [d] shnysct@gmail.com, [e] hongchao@njust.edu.cn, [f] zhangaijun@njust.edu.cn, [g] sokolov@gsu.by

Получено 20.09.2026, после доработки — 09.10.2026.
Принято к публикации 10.10.2026.

Работа посвящена суррогатному моделированию термомеханических откликов процесса лазерной полировки кварцевого стекла по данным конечно-элементных расчетов. Исследуется зависимость температурных и механических характеристик процесса от мощности лазерного излучения, скорости перемещения источника и радиуса лазерного пятна. Для аппроксимации откликов сопоставлены классические и регуляризованные регрессионные модели, методы опорных векторов, ансамбли деревьев решений, физически структурированные модели, тензорные B-сплайны и эволюционно синтезированные нейронные сети. Сравнение выполнено при едином разбиении исходных данных на обучающую, валидационную и независимую тестовую выборки. Наименьшие ошибки прогнозирования для всех исследованных откликов обеспечили стекинг-ансамбли на основе Random Forest, Gradient Boosting и XGBoost; коэффициенты детерминации на тестовой выборке превышали 0,998. Физически структурированные модели уступали ансамблям по абсолютной точности, однако обеспечивали гладкое и интерпретируемое представление зависимостей между параметрами лазерного воздействия и термомеханическими откликами. Эволюционный поиск позволил получить нейросетевую модель с двумя выходами для совместного прогнозирования максимальной температуры и максимального эквивалентного напряжения. В исследованном наборе данных скорость перемещения источника имеет наибольшую перестановочную значимость для качества прогнозирования выбранных моделей. Результаты исследования показывают, что выбор суррогатной модели должен определяться решаемой задачей: ансамблевые модели целесообразны для высокоточного прогнозирования, физически структурированные — для анализа зависимостей и интерпретации, нейросетевые — для совместного прогнозирования взаимосвязанных откликов. Построенные модели могут служить вычислительной основой для анализа режимов и последующей многокритериальной оптимизации лазерной полировки кварцевого стекла.

Ключевые слова: лазерная полировка, кварцевое стекло, конечно-элементное моделирование, термовязкоупругость, суррогатная модель, физически структурированные признаки, тензорные B-сплайны, ансамблевое обучение, нейроэволюция

© 2026 Лариса Николаевна Марченко, Юрий Валерьевич Никитюк, Юлия Викторовна Бруттан, Владислав Александрович Прохоренко, Хунчао Чжан, Айцзюнь Чжан, Сергей Иванович Соколов
Статья доступна по лицензии Creative Commons Attribution-NoDerivs 3.0 Unported License.
Чтобы получить текст лицензии, посетите веб-сайт http://creativecommons.org/licenses/by-nd/3.0/
или отправьте письмо в Creative Commons, PO Box 1866, Mountain View, CA 94042, USA.

Introduction

Quartz glass, owing to its high thermal resistance, chemical inertness, low coefficient of thermal expansion, and transparency over a wide spectral range, is widely used in laser and optical electronic systems, microelectronics, instrumentation, and other high-technology fields. At the same time, the service life and optical strength of products largely depend on surface quality: microcracks, scratches, contamination, and residual stresses arising after mechanical processing degrade optical characteristics and reduce the resistance of the material to intense laser radiation [Arbuzov, 2008; Shershnev et al., 2015].

Laser polishing of quartz glass is a non-contact finishing method in which CO_2-laser radiation is absorbed in a thin surface layer and causes local melting. Under the action of surface-tension forces in the resulting molten micropool, the initial microtopography is smoothed, making it possible to achieve the required roughness level and effectively remove residual defects left after preliminary processing. The possibility of effectively reducing the roughness of quartz surfaces and microoptical components was shown in early experimental and technological studies [Sysoev, 2003; Nowak et al., 2006; Hildebrand et al., 2011; Hildebrand et al., 2012]. In particular, the formation of a supersmooth surface was demonstrated for fused quartz, and modeling confirmed the determining role of surface tension in the smoothing mechanism [He et al., 2018]. Optimization of regimes by the Taguchi method also showed a significant influence of radiation power, scanning speed, and trajectory parameters on the final roughness [Lu et al., 2024].

A technologically stable regime exists only within a limited parameter domain. The surface temperature must provide the required reduction in viscosity but must not lead to intense evaporation, changes in macrogeometry, thermal cracking, or inadmissible residual stresses. Therefore, power P, travel speed V, and spot radius R must be analyzed jointly: they determine the average power density, the characteristic time of local exposure, and the energy supplied per unit path length and surface area.

Experimental investigation of the entire range of regimes requires substantial effort and does not always allow internal temperature and mechanical fields to be recorded. For this reason, finite-element modeling is one of the primary analysis tools, providing the calculation of nonstationary temperatures, strains, and stresses within the product volume. Finite-element models of laser processing of glass have been used to study polishing, controlled thermal splitting, and the selection of technological parameters [Shershnev et al., 2015; Emelyanov et al., 2022; Nisar, 2025]. In [Nikityuk et al., 2026], a model of laser polishing of quartz glass in ANSYS was constructed and verified; based on its results, a dataset of temperatures and equivalent stresses was formed for different combinations of processing parameters.

The high informativeness of a direct finite-element calculation is combined with its considerable computational cost. When planning computational experiments, analyzing sensitivity, assessing stability, and performing multicriteria optimization, repeated calls to the model are required; therefore, a full thermomechanical calculation for each new combination of factors requires substantial resources. Surrogate modeling is used to remove this limitation: the expensive finite-element model is replaced by a computationally efficient surrogate dependence trained on the results of previously performed calculations. Theoretical foundations of this approach were laid in works on the design of computer experiments, response surfaces, and surrogate optimization [Sacks et al., 1989; Simpson et al., 2001; Queipo et al., 2005; Forrester, Keane, 2009; Jiang et al., 2020].

Polynomial regressions, Gaussian processes, support-vector methods, splines, tree ensembles, and neural networks differ in accuracy, smoothness, stability, and interpretability. Surrogate models are used for accelerated prediction of temperature fields and residual stresses in laser-processing processes [Li, Polydorides, 2022; Dong et al., 2022; Hemmasian et al., 2023]. Multicriteria surrogate optimization of laser polishing of additively manufactured parts made it possible to reduce roughness

and the size of the heat-affected zone simultaneously [Solheid et al., 2022]. Therefore, a similar approach is also promising for selecting quartz-glass processing regimes, although the transfer of conclusions between materials requires separate physical verification.

Quadratic response-surface modeling has also been used to optimize laser-polished surface topography while accounting for the initial surface [Rosa et al., 2014]. A review of laser-polishing models for metallic materials discusses the simplifying assumptions and validation challenges of thermophysical descriptions [Mohajerani et al., 2018]. Bayesian optimization has been applied to laser cutting, welding, and polishing [Menold et al., 2024].

For interpretable models, the choice of physically meaningful features is important. Ridge regression stabilizes estimates under correlated predictors [Hoerl, Kennard, 1970], Lasso performs shrinkage and feature selection [Tibshirani, 1996], and Elastic Net combines L1 and L2 penalties [Zou, Hastie, 2005]. SVR describes smooth nonlinear dependences [Smola, Schölkopf, 2004], Random Forest and gradient boosting account for factor interactions [Breiman, 2001; Friedman, 2001; Chen, Guestrin, 2016], and stacking combines mutually complementary predictions of base algorithms [Wolpert, 1992]. Penalized B-splines provide a smooth nonlinear representation of the response with controlled complexity [Eilers, Marx, 1996]. The use of physically motivated transformations is consistent with the concept of physics-informed and theory-guided machine learning [Raissi et al., 2019; Karniadakis et al., 2021].

For a number of laser-processing tasks for silicate and quartz glasses, regression, neural-network, and fuzzy models, as well as algorithms for multicriteria optimization of technological parameters, have been developed [Nikityuk et al., 2023; Nikityuk et al., 2024; Nikityuk et al., 2026]. However, there is no unified comparison of a broad set of models on the same responses of a calibrated thermomechanical model while simultaneously accounting for interpolation accuracy, physical interpretability, and computational applicability.

The aim of this study is to develop and compare surrogate models of thermomechanical responses of quartz-glass laser polishing constructed from the data of a calibrated finite-element model.

To achieve this aim, the following tasks are solved.

1. To construct physically justified models of temperatures and stresses based on finite-element calculation results and evaluate them on an independent test sample using R^2 and R^2_{adj}, as well as RMSE, MAE, and MAPE.

2. To compare classical and regularized regressions, support-vector methods, ensemble algorithms, physics-structured models, tensor B-splines, and physics-guided neural networks in terms of accuracy, stability, interpretability, interpolation accuracy within the investigated parameter domain, and computational cost.

3. To study the applicability of evolutionary methods for synthesizing an optimal neural-network architecture to approximate the responses of the physical process of quartz-glass laser polishing.

4. To determine the class of surrogate models most suitable by the set of evaluation metrics for use in approximating responses of finite-element models and in multicriteria optimization of laser-polishing parameters by genetic algorithms.

The study considers a unified set of surrogate approximators: physically motivated logarithmic quadratic regression PhysicalLogQuadratic; the quadratic least-squares model QuadraticOLS; regularized Ridge, Lasso, and Elastic Net models; physics-structured regressions PhysicalRidge and PhysicalRidgeLog1p; GAM-like models based on tensor B-splines, TensorSplineGAM and TensorSplineGAMLog1p; support-vector regression with linear, polynomial, and radial-basis kernels; Random Forest; Gradient Boosting and XGBoost; a stacking ensemble with a Ridge-CV regression metamodel; and physics-guided neural networks whose architecture is synthesized by an evolutionary algorithm with NSGA-II multicriteria selection [Deb et al., 2002]. Hyperparameters are selected using cross-validation, validation, and independent test samples.

The scientific novelty lies in the coordinated comparison of different surrogate models on a unified set of thermomechanical responses, in the introduction of physically interpretable combinations of moving-source parameters, in the use of tensor spline interactions, and in the multicriteria evolutionary synthesis of a two-output neural architecture.

The results obtained are intended for a reasonable selection of a surrogate model that can accurately predict temperature and thermomechanical responses of laser polishing in the investigated parameter domain, while maintaining a low computational cost. This model will also serve as a foundation for future multicriteria optimization of the process.

Physical and mathematical model of quartz glass laser polishing

A sequential one-way coupled thermoviscoelastic model of the thermal cycle is considered. The temperature field determines thermal strains and stresses, whereas the inverse influence of the mechanical state on heat transfer is neglected. The motion of softened material, changes in the free surface, surface tension, the Marangoni effect, and evaporation are not included in the calculation. The model is intended for calculating temperatures and stresses.

A plate is considered with length L_x, width L_z, and height H:

$$\Omega = \{(x,\, y,\, z)\colon 0 < x < L_x,\ 0 < y < H,\ 0 < z < L_z\},$$

where $L_x = 0.06$ m and $L_z = 0.02$ m. Neglecting the change in density due to thermal expansion, the temperature field satisfies the equation

$$\rho_0 c_p(T)\frac{\partial T}{\partial t} - \nabla \cdot [k(T)\nabla T] = 0, \quad x \in \Omega, \quad T(x,\, 0) = T_0 = 293 \text{ K},$$

where ρ_0 is the accepted constant density, c_p is the specific heat capacity, and $k(T)$ is the thermal conductivity.

The laser source successively occupies N positions. On the interval, the active circular region is

$$\Gamma_{L,i} = \left\{(x,\, 0,\, z)\colon (x - x_i)^2 + (z - z_0)^2 \leqslant R_{eff,i}^2\right\},$$
$$x_i = x_0 + i\,\Delta x, \quad R_{eff,i} = K_{R,i}R_i, \quad t_{i+1} - t_i = \frac{\Delta x}{V_i}.$$

The absorbed surface flux is specified by a top-hat profile

$$q_i = \frac{\eta_i P_i}{\pi R_{eff,i}^2}, \quad \eta_i = K_{SRC,i}K_{PROFILE,i}(1 - K_2).$$

The coefficient $K_{SRC,i}$ corrects the effective absorbed source power, $K_{PROFILE,i}$ accounts for replacing the measured spatial profile by an idealized top-hat profile, $K_{R,i}$ sets the effective spot radius, and K_2 is the accepted reflection coefficient. These coefficients were not reestimated when constructing the surrogates; they were fixed from the calibration results of the initial finite-element model [Nikityuk et al., 2026]. For an outward normal n, the heating condition on the irradiated surface has the form

$$-k(T)\nabla T \cdot n = -q_i \quad \text{on } \Gamma_{L,i},$$

whereas the remaining faces are assumed to be thermally insulated while the source passes. After heating is completed, radiative cooling is specified on the entire surface:

$$-k(T)\nabla T \cdot n = \varepsilon_r \sigma_{SB}\left(T^4 - T_\infty^4\right),$$

where epsilon is the emissivity, $\varepsilon_r = 0.91$, $\sigma_{SB} = 5.67 \cdot 10^{-8}$ W/$\left(\text{m}^2 \cdot \text{K}^4\right)$, and $T_\infty = 293$ K is the ambient temperature. The initial temperature of the plate is also 293 K. The calculated cooling duration is 1000 s; convective heat transfer is not included in the adopted model.

Quasistatic mechanical equilibrium is described by the relations

$$\nabla \cdot \sigma = 0, \quad \varepsilon = \frac{1}{2}\left(\nabla u + \nabla u^T\right),$$
$$\varepsilon^{th} = \alpha(T - T_{ref})I, \quad \alpha = 5.5 \cdot 10^{-7}\ \text{K}^{-1}.$$

The volumetric component of deformation is assumed to be elastic, and the deviatoric component is assumed to be linearly viscoelastic. The instantaneous bulk and shear moduli are defined as

$$K_b(T) = \frac{E(T)}{3[1 - 2\nu(T)]}, \quad G_0(T) = \frac{E(T)}{2[1 + \nu(T)]},$$

where $E(T)$ and $\nu(T)$ are the temperature-dependent Young modulus and Poisson ratio. The shear relaxation function is specified by a one-term Prony series

$$G(\Delta\xi, T) = G_0(T)\left[g_\infty + g_1 \exp\left(\frac{-\Delta\xi}{\tau_1}\right)\right],$$
$$g_1 = 0.572, \quad g_\infty = 1 - g_1, \quad \tau_1 = 5.5 \cdot 10^{-4}\ \text{s}.$$

The reduced time is defined by the expression

$$\xi(t) = \int_0^t \frac{d\tau}{a_T[T(\tau)]}.$$

Since the temperature-time shift is not used, $a_T \equiv 1$ and $\xi = t$. The mechanical problem is solved successively over time steps while preserving the internal variables of the Prony series. The initial state at $T = T_{ref}$ is assumed to be stress-free. Inertial and body forces are neglected, free surfaces are assigned zero tractions $\sigma n = 0$, and the minimum kinematic constraints eliminate only the six rigid-body modes.

For an admissible test function, the weak form of the thermal problem is

$$\int_\Omega \rho_0 c_p(T)\dot{T} w\, d\Omega + \int_\Omega k(T)\nabla T \cdot \nabla w\, d\Omega + \int_{\Gamma_{rad}} \varepsilon_r \sigma_{SB}\left(T^4 - T_\infty^4\right) w\, d\Gamma = \int_{\Gamma_L} q_L w\, d\Gamma,$$

and the weak form of mechanical equilibrium is written as

$$\int_\Omega \sigma : \delta\varepsilon\, d\Omega = 0.$$

These relations form the basis of the sequential finite-element implementation of the thermal and viscoelastic mechanical problems.

Finite-element modeling and generation of initial data for surrogate models

The process of laser heating of quartz glass was studied using the scheme shown in Fig. 1. The laser-radiation spot (1) on the quartz plate (2) has the shape of a circle. The arrows indicate the directions of beam motion relative to the specimen surface, and the parameter S corresponds to the scanning step.

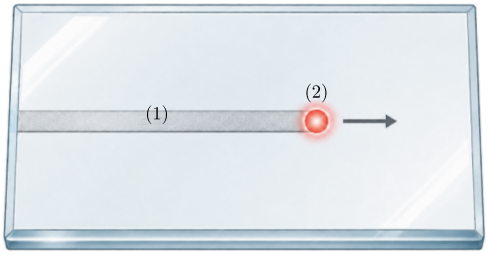


Figure 1. Scheme of laser-beam motion: (1) laser spot; (2) quartz plate

The calculation was performed in ANSYS Mechanical APDL as a sequence of thermal and structural solutions on a common three-dimensional mesh. A plate of the specified size was discretized by a regular mesh of eight-node hexahedra with a step of 0.25 mm in the x and z directions and 0.5 mm through the thickness; the mesh contains 14 400 elements. SOLID70 elements were used at the thermal stage, and the corresponding eight-node SOLID185 elements were used for the structural solution. Thermophysical and elastic properties were specified as tabulated functions of temperature. Material parameters, thermal-source calibration, and comparison with experimental temperature observations are given in [Nikityuk et al., 2026].

A total of 1185 unique regimes were formed on the grid of the computational experiment. The input parameters of the modeled physical process were the laser spot radius R (mm), power P (W), and travel speed V (mm/s), with variation ranges R = 2–3 mm, P = 40–60 W, and V = 1–3 mm/s. The number of regimes for each radius ranged from 234 to 239. The responses were the maximum temperature $T_{\max}$ (K) and maximum equivalent stress $\sigma_{\max}$ (MPa) during heating, as well as the temperature T_{cool} (K) and equivalent stress σ_{cool} (kPa) after 1000 s of cooling (Table 1).

Table 1. Experimental design and calculation results

Response	Range
$T_{\max}$, K	1413.55–2462.65
$\sigma_{\max}$, MPa	20.956–60.737
T_{cool}, K	442.36–1087.13
σ_{cool}, kPa	97.601–147.153
Training / validation / test samples	711 / 237 / 237 regimes

The set of unique observations was divided into training, validation, and independent test samples in a 60 : 20 : 20 ratio. Preprocessing parameters and model coefficients were estimated without using test data. Hyperparameters were selected by five-fold cross-validation within the training part.

Regression models studied for quartz glass laser polishing

To approximate the responses of the finite-element model, classical regression, ensemble, and physics-structured surrogate models were used. The vector of initial technological factors was specified as

$$x = (P, V, R)^T,$$

where P is the laser-radiation power, V is the source travel speed, and R is the laser spot radius. The responses considered were the maximum temperature during heating $T_{\max}$, the temperature after cooling T_{cool}, the maximum equivalent stress $\sigma_{\max}$, and the equivalent stress after cooling σ_{cool}.

The first group of surrogate models consisted of classical regression and ensemble models.

Quadratic regression estimated by least squares has the form

$$\widehat{y} = \beta_0 + \sum_{j=1}^{m} \beta_j x_j + \sum_{j=1}^{m} \beta_{jj} x_j^2 + \sum_{j<k} \beta_{jk} x_j x_k = \phi(x)^T \beta,$$

where $m = 3$ and $\phi(x)$ is the vector of basis functions, and β contains the intercept, linear, quadratic, and pairwise interaction components. For a complete quadratic basis in the factors P, V and R, the number of regression terms without the intercept is nine.

Ridge, Lasso, and Elastic Net regressions were defined from the common regularized problem

$$\widehat{\beta} = \arg\min_{\beta} \left\{ \frac{1}{n} \sum_{i=1}^{n} \left(y_i - \phi_i^T \beta \right)^2 + \lambda \left[\frac{1-\eta}{2} \| \beta \|_2^2 + \eta \| \beta \|_1 \right] \right\},$$

where $\eta \geqslant 0$ is the regularization parameter. The case $\eta = 0$ corresponds to Ridge regression, $\eta = 1$ to Lasso regression, and $0 < \eta < 1$ to Elastic Net [Hoerl, Kennard, 1970; Tibshirani, 1996; Zou, Hastie, 2005]. The intercept was not regularized. Standardization was estimated separately inside each training fold.

Support-vector regression (SVR) was studied with linear, polynomial, and radial-basis kernels. In general form, the model minimizes a regularized ε-insensitive loss function

$$\min_{f \in H} \left\{ \frac{1}{2} \| f \|_H^2 + C \sum_{i=1}^{n} L_\varepsilon (y_i - f(x_i)) \right\},$$

$$L_\varepsilon(e) = \max(0, |e| - \varepsilon),$$

where C determines the trade-off between smoothness and error, and ε is the width of the insensitive zone [Smola, Schölkopf, 2004].

For Random Forest, the prediction was defined by averaging the outputs of M trees

$$\widehat{y}(x) = \frac{1}{M} \sum_{m=1}^{M} h_m(x).$$

Gradient Boosting and XGBoost formed an additive ensemble of trees

$$F_M(x) = F_0(x) + \sum_{m=1}^{M} \nu \gamma_m h_m(x),$$

where h_m is the base tree, ν is the learning rate, and γ_m is the weight of the added tree.

In XGBoost, the loss function is supplemented by a penalty for tree complexity [Breiman, 2001; Friedman, 2001; Chen, Guestrin, 2016].

Stacking used Random Forest, Gradient Boosting, and XGBoost. For each base algorithm, the development set was divided into K folds; the prediction for an object was formed by a model that had not been trained on this object. The resulting out-of-fold matrix $Z \in R^{n \times 3}$ served as the input to the Ridge metamodel

$$\widehat{y} = \beta_0 + z^T \beta.$$

After estimating the metamodel, the base algorithms were retrained on the full development set. This scheme prevents leakage of the target value into the metamodel features [Wolpert, 1992].

The second group consisted of physics-structured models. In the physics-structured block, the original factors were supplemented by combinations $\frac{P}{\pi R^2}$, $\frac{R}{V}$, $\frac{P}{V}$, $\frac{P}{RV}$, VR, $\frac{PR}{V}$ that were treated as proxy variables characterizing, respectively, the average intensity of exposure, the characteristic time of spot passage, the line energy, the surface energy density, the scale ratio between convective motion of the source and thermal diffusion, and the energy supplied during the time in which the source travels a distance of order R. The product VR is not a Peclet number in the strict sense, since the dimensionless Peclet number is defined as $Pe = \frac{VR}{a}$, where a is the thermal diffusivity of the material.

To preserve dimensional correctness, logarithmic features were defined through fixed unit scales:

$$l_P = \ln \frac{P}{P_0}, \quad l_V = \ln \frac{V}{V_0}, \quad l_R = \ln \frac{R}{R_0},$$

where $R_0 = 1$ mm, $P_0 = 1$ W, and $V_0 = 1$ mm/s. Thus, the numerical values of the logarithms coincide with the logarithms of the factors expressed in the specified units.

The PhysicalRidge model was a Ridge regression on an extended physically motivated basis.

For positive responses, the following transformation was additionally used

$$z = \ln\left(1 + \frac{y}{y_0}\right), \quad \widehat{y} = y_0[\exp(\widehat{z}) - 1],$$

where $y_0 = 1$ K for temperatures and $y_0 = 1$ Pa for stresses. The constraint $\widehat{y} \geqslant 0$ was introduced after the inverse transformation.

The smooth tensor B-spline model was written as

$$\widehat{y} = \beta_0 + \sum_j f_j(x_j) + \sum_{j<k} f_{jk}(x_j, x_k),$$

or, in matrix form,

$$\widehat{y} = c + a_R^T B_R + a_P^T B_P + a_V^T B_V + B_R^T M_{RP} B_P + B_R^T M_{RV} B_V + B_P^T M_{PV} B_V.$$

The coefficients were estimated from the penalized problem

$$\widehat{\theta} = \arg\min_{\theta} \left\{ \|y - X_B\theta\|_2^2 + \lambda \|L\theta\|_2^2 \right\},$$

where X_B is the spline design matrix and L specifies the penalty for coefficient complexity [Eilers, Marx, 1996].

The number of knots, spline degree, presence of pairwise tensor interactions, and λ were selected by cross-validation.

Hyperparameters were selected only from the training data using five-fold cross-validation. For the physics-structured block, a separate validation sample was used to choose the model family, basis composition, and response scale. After choosing the configuration, the model was retrained on the combined training and validation samples and evaluated once on the independent test sample containing 237 regimes. The test data were not used when selecting features, transformations, or hyperparameters.

The reported validation and test results characterize prediction within the sampled parameter domain.

Synthesis of an optimal neural-network model for response approximation

In addition to the regression models presented above, a multicriteria neuroevolutionary algorithm for automated architecture search was applied [Nikityuk et al., 2023; Stanley, Miikkulainen, 2002; Deb et al., 2002; Elsken et al., 2019]. The search criterion was to provide the best compromise between approximation accuracy and computational efficiency.

The unit of evolutionary search was a neural-network architecture represented by a directed acyclic graph of large functional blocks. The graph included an input node containing the problem factors, namely, laser-radiation power P, travel speed V, and spot radius R; deterministic physically motivated blocks forming energetic, temporal, and thermophysical combinations of the original factors; and trainable fully connected blocks containing from one to several Dense layers of small dimension. The output part of the network was organized as a two-channel thermomechanical block forming predictions of the maximum temperature $T_{\max}$ and the maximum equivalent stress $\sigma_{\max}$, with the temperature representation additionally passed to the mechanical branch. This construction preserved an interpretable connection with the process physics and at the same time allowed both sequential and branched computational graphs to be formed.

Quality metrics

The independent test sample served as the basis for comparing the calculated values from finite-element modeling with the responses of the surrogate models.

To evaluate the combined influence of the input parameters on the response, the coefficient of determination was used and was defined as

$$R^2 = 1 - \frac{\sum\limits_{i=1}^{n_{test}} (y_i - \widehat{y}_i)^2}{\sum\limits_{i=1}^{n_{test}} (y_i - \overline{y})^2}, \quad \overline{y} = \frac{1}{n_{test}} \sum_{i=1}^{n_{test}} y_i.$$

Absolute errors were characterized by the metrics

$$MAE = \frac{1}{n_{test}} \sum_{i=1}^{n_{test}} |y_i - \widehat{y}_i|, \quad RMSE = \sqrt{\frac{1}{n_{test}} \sum_{i=1}^{n_{test}} (y_i - \widehat{y}_i)^2}.$$

A normalized error was used to compare responses of different scales

$$NRMSE = \frac{RMSE}{y_{\max} - y_{\min}} \cdot 100\,\%.$$

Relative errors were calculated using the formulas

$$MAPE = \frac{100\,\%}{n_{nz}} \sum_{i:\, y_i \neq 0} \left| \frac{y_i - \widehat{y}_i}{y_i} \right|,$$

$$sMAPE = \frac{100\,\%}{n_{test}} \sum_{i=1}^{n_{test}} \frac{2|y_i - \widehat{y}_i|}{|y_i| + |\widehat{y}_i|}.$$

Here n_{nz} is the number of nonzero actual values. If $y_i = \widehat{y}_i = 0$, the corresponding sMAPE term was set equal to zero. MAPE was used only for positive responses that did not approach zero.

For unregularized linear models on the training data, the adjusted coefficient of determination was additionally calculated

$$R^2_{adj} = 1 - \left(1 - R^2_{train}\right) \frac{n_{train} - 1}{n_{train} - p - 1},$$

where p is the number of estimated regression terms without the free coefficient. For Ridge and spline models, the effective number of degrees of freedom was used

$$p_{eff} = \mathrm{tr}(H).$$

The adjusted coefficient of determination was calculated in the unified table as $R^2_{adj,common}$ over the three original technological factors for all models. For regularized and spline models, auxiliary estimates related to the effective complexity of the approximator were additionally saved.

Confidence intervals of the test metrics were determined by paired nonparametric bootstrap over $B = 1000$ repeated samples of pairs $(y_i, \widehat{y}_i)$. The 95 % interval bounds corresponded to the 2.5th and 97.5th percentiles of the bootstrap distribution of the metric [Efron, Tibshirani, 1993].

Numerical experiment methodology

The computational part was implemented in Python. SciPy was used for scientific and statistical calculations [Virtanen et al., 2020], scikit-learn for preprocessing pipelines, cross-validation, and most regression algorithms [Pedregosa et al., 2011], XGBoost for extreme gradient boosting [Chen, Guestrin, 2016], statsmodels package for diagnostic procedures [Seabold, Perktold, 2010], and TensorFlow/Keras for the neural-network experiment [Abadi et al., 2016].

Hyperparameters of the regression models were selected on the training part by five-fold cross-validation with RMSE minimization. After tuning, the models were evaluated on the validation sample; the type of model included in the final comparison was fixed by the validation criterion. The chosen configuration was then retrained on the union of the training and validation parts and evaluated once on the independent test sample of 237 regimes. Thus, the classical, ensemble, and physics-structured models were compared on exactly the same data split.

Hyperparameters of PhysicalRidge and PhysicalRidgeLog1p, which use physically interpretable combinations of the original speed (V), power (P), and radius (R) factors together with the factors themselves, were selected on the training part by five-fold cross-validation. The tuned models were checked on the validation sample, retrained on the union of training and validation data, and only then evaluated on the test part. For GAM-like models, the number of spline-grid knots varied from 3 to 7, and the spline degree was 2 or 3. Both the additive mode and the pairwise-interaction mode were compared; coefficients were estimated with a Ridge penalty, and TensorSplineGAM and TensorSplineGAMLog1p variants were also analyzed.

The evolutionary search for a neural-network architecture was performed on the same data split as the other compared models. Five independent runs were performed with a population of 40 individuals, 20 generations, and 40 offspring in each generation; in total, 4200 candidates were evaluated, all of which were completed with status ok. The test sample was not used in the evolution: candidates were trained on the training part and compared by validation metrics; after the architecture was fixed, the model was trained on the union of train and validation and then checked on the test sample.

Results of the numerical experiment and discussion

The comparison was performed for classical regression and ensemble algorithms, physics-structured regularized and spline models, and evolutionarily synthesized neural networks. In all cases, the same initial set of 1185 unique laser-polishing regimes and a common 711/237/237 split were used. For non-NAS models, four responses were predicted, whereas for NAS, two heating-stage responses, $T_{\max}$ and $\sigma_{\max}$, were predicted [Nikitjuk et al., 2026].

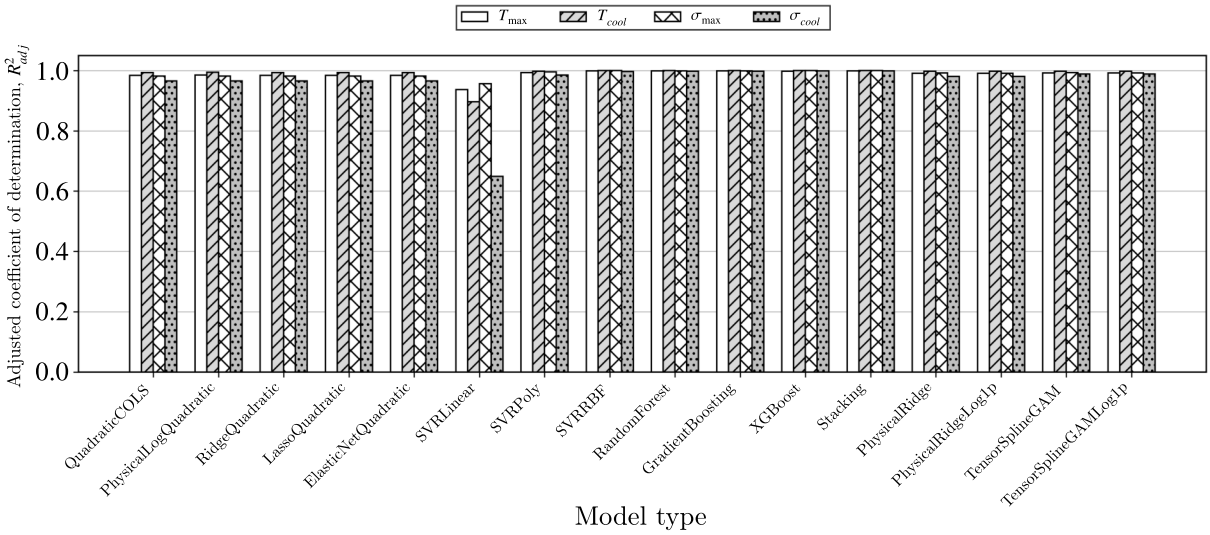


Figure 2. Adjusted coefficient of determination R^2_{adj} on the common validation sample for 16 surrogate models and four finite-element responses. The same adjustment over three original factors is used for all models; higher values indicate closer agreement

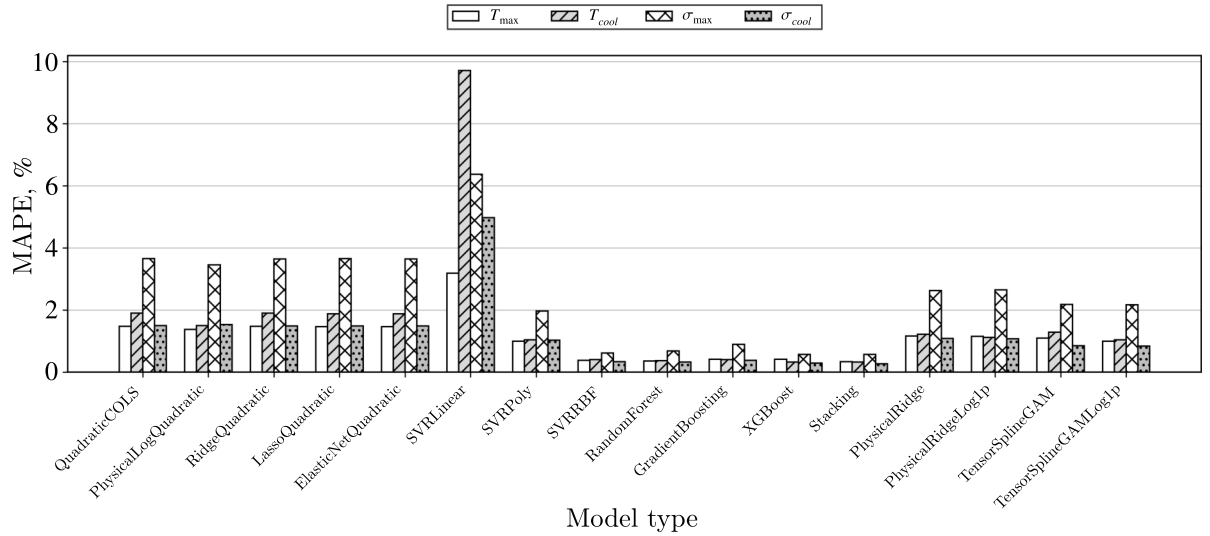


Figure 3. Mean absolute percentage error (MAPE) on the common validation sample for 16 surrogate models and four finite-element responses. Hatching identifies the responses; lower values indicate smaller relative prediction errors

Figures 2–4 compare the validation values of the adjusted coefficient of determination, MAPE, and sMAPE for all 16 non-NAS models and four responses (237 validation regimes). The adjusted

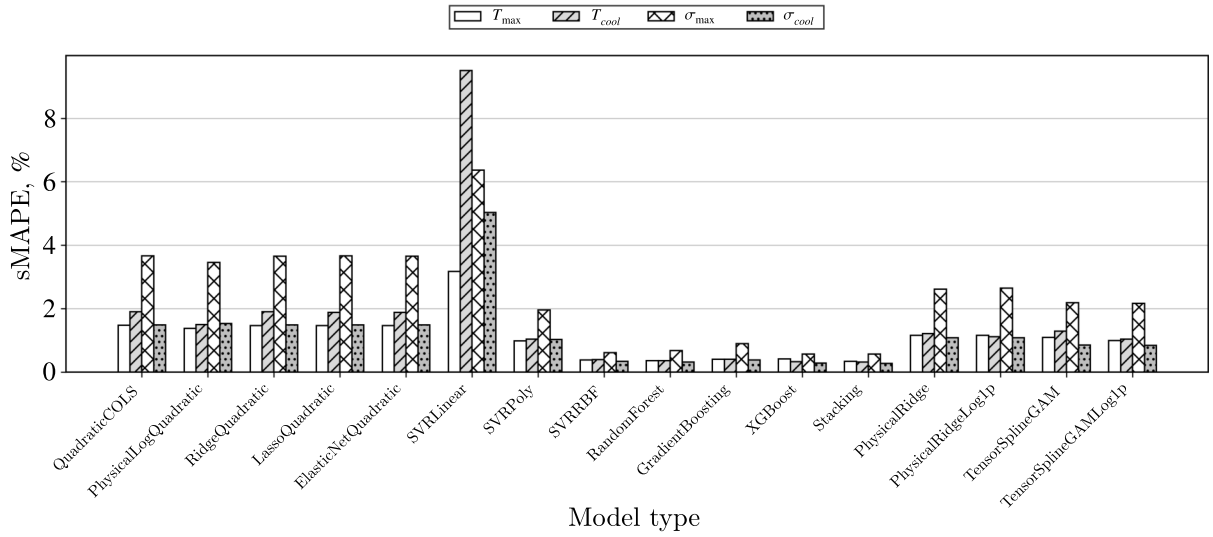


Figure 4. Symmetric mean absolute percentage error (sMAPE) on the common validation sample for 16 surrogate models and four finite-element responses. The model order and hatching match Figs. 2 and 3; lower values indicate smaller relative prediction errors

coefficient is calculated uniformly using the three original factors. These plots refer to model selection before refitting on the combined training and validation data; the tables below report the subsequent independent test results. PhysicalNAS is omitted because its experiment covers only the two heating-stage responses.

Classical regression and ensemble models

Among the classical and ensemble methods, the best results according to the validation criterion for all four responses were obtained by a stacking ensemble combining Random Forest, Gradient Boosting, and XGBoost with a Ridge-CV regression metamodel (Table 2).

Table 2. Quality of the best classical and ensemble models on the test sample

Response	Selected model	R^2	RMSE	MAE	MAPE, %	NRMSE, %
T_{max}	Stacking	0.999356	7.198 K	4.001 K	0.208	0.694
T_{cool}	Stacking	0.999840	2.643 K	1.456 K	0.200	0.413
σ_{max}	Stacking	0.999725	0.225 MPa	0.135 MPa	0.375	0.574
σ_{cool}	Stacking	0.998735	0.483 kPa	0.219 kPa	0.179	1.022

For the selected stacking model for T_{max}, the 95 % bootstrap interval of RMSE was 5.447–8.847 K, and the MAPE interval was 0.170–0.249 %. For σ_{max}, the corresponding 95 % RMSE interval was 0.174–0.276 MPa, and the MAPE interval was 0.313–0.450 %. For T_{cool}, the minimum validation error and final test RMSE of 2.643 K were obtained by stacking.

The final stacking models were built according to a common scheme: the base regressors comprised Random Forest, Gradient Boosting, and XGBoost, and their out-of-fold predictions were fed into a Ridge-CV regression metamodel. After the hyperparameters were selected on the training folds, the entire configuration was retrained on the union of the training and validation samples.

The composition of the selected stacking models is given in Table 3.

The metrics values (Table 2) show that, under the common split, stacking ensembles provide the lowest errors among the regression models for all four responses of the finite-element model.

Table 3. Composition of the selected stacking models

Response	Base models	Metamodel	Selection criterion
$T_{\max}$	Random Forest; Gradient Boosting; XGBoost	RidgeCV	minimum RMSE on validation
T_{cool}	Random Forest; Gradient Boosting; XGBoost	RidgeCV	minimum RMSE on validation
$\sigma_{\max}$	Random Forest; Gradient Boosting; XGBoost	RidgeCV	minimum RMSE on validation
σ_{cool}	Random Forest; Gradient Boosting; XGBoost	RidgeCV	minimum RMSE on validation

Physics-structured regularized models

In the physics-structured block, TensorSplineGAMLog1p models were selected by the validation criterion for $T_{\max}$, T_{cool}, and σ_{cool}, whereas TensorSplineGAM was selected for the maximum heating stress $\sigma_{\max}$ (Table 4).

Table 4. Quality of the best physics-structured models on the test sample

Response	Selected model	R^2	R^2_{adj}	RMSE	MAE	MAPE, %	NRMSE, %
$T_{\max}$	TS-GAMLog1p	0.992468	0.992371	24.612 K	17.506 K	0.890	2.373
T_{cool}	TS-GAMLog1p	0.997563	0.997532	10.310 K	7.086 K	0.979	1.610
$\sigma_{\max}$	TS-GAM	0.993348	0.993262	1.105 MPa	0.735 MPa	1.968	2.826
σ_{cool}	TS-GAMLog1p	0.991199	0.991086	1.273 kPa	0.892 kPa	0.689	2.696

The R^2_{adj} values reported in Table 4 were calculated uniformly across the three original technological factors for all compared models. All other metrics were computed using the same metric functions as for the ensemble models.

Coefficient forms of the selected temperature models TensorSplineGAMLog1p were obtained from serialized models of the current calculation. The construction of both models relied on B-spline bases with linear extrapolation. Coefficient vectors, pairwise-interaction matrices, intercepts, and regularization parameters for all four selected physics-structured models are provided in Appendix A (Tables A1–A16).

The linear form is

$$\eta = c + a_R^T B_R + a_P^T B_P + a_V^T B_V + B_R^T M_{RP} B_P + B_R^T M_{RV} B_V + B_P^T M_{PV} B_V.$$

Comparison of accuracy and interpretability

A direct comparison of models selected by the validation criterion in the ensemble and physics-structured blocks is given in Table 5. The RMSE ratio characterizes how many times the root-mean-square error of the selected physics-structured model is greater than the error of the selected stacking ensemble with a Ridge-CV regression metamodel on the same test sample.

Table 5. Comparison of the best ensemble and physics-structured models

Response	Best ensemble model	Best physical model	Ensemble RMSE	Physical-model RMSE	RMSE ratio
$T_{\max}$	Stacking	TS-GAMLog1p	7.198 K	24.612 K	3.419
T_{cool}	Stacking	TS-GAMLog1p	2.643 K	10.310 K	3.901
$\sigma_{\max}$	Stacking	TS-GAM	0.225 MPa	1.105 MPa	4.921
σ_{cool}	Stacking	TS-GAMLog1p	0.483 kPa	1.273 kPa	2.638

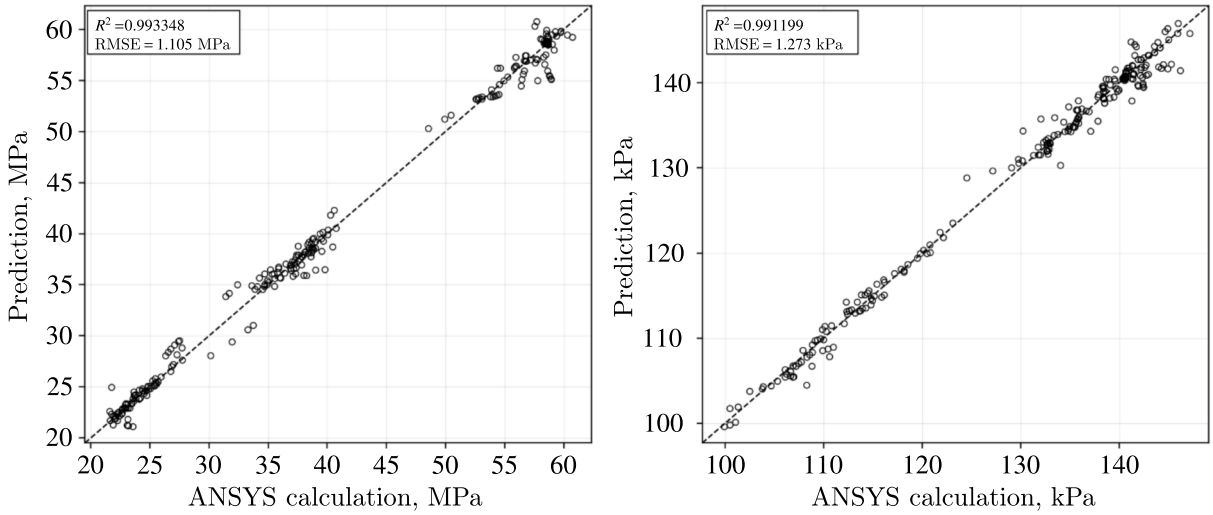
Under the common split, the physics-structured models had RMSE values approximately 2.638–4.921 times higher than stacking. The largest difference was obtained for $\sigma_{\max}$, where

TensorSplineGAM gave an error 4.921 times greater than stacking; the smallest difference was observed for σ_{cool} (2.638 times). Therefore, the advantage of ensembles in terms of minimum test error is retained for all responses considered.

The advantage of ensembles is explained by their ability to flexibly reproduce local nonlinearities and factor interactions without specifying a fixed analytical structure. At the same time, physics-structured models have two important merits. First, they directly link the prediction to the energetic and temporal characteristics of laser exposure. Second, the smooth response form facilitates derivative analysis, construction of response surfaces, and use of gradient or multicriteria optimization methods.

Thus, within the investigated factor domain, stacking ensembles provide the highest accuracy among non-NAS models. TensorSplineGAMLog1p and TensorSplineGAM are appropriate as interpretable smooth models for factor analysis, local derivatives, and construction of response surfaces, but not as models with minimum test error.

Figure 5 shows a comparison of calculated and predicted stresses for the physics-structured models; most points lie near the ideal-agreement line, although local regions of increased error remain. Therefore, the figure should be interpreted as a parity diagram rather than as a residual plot.



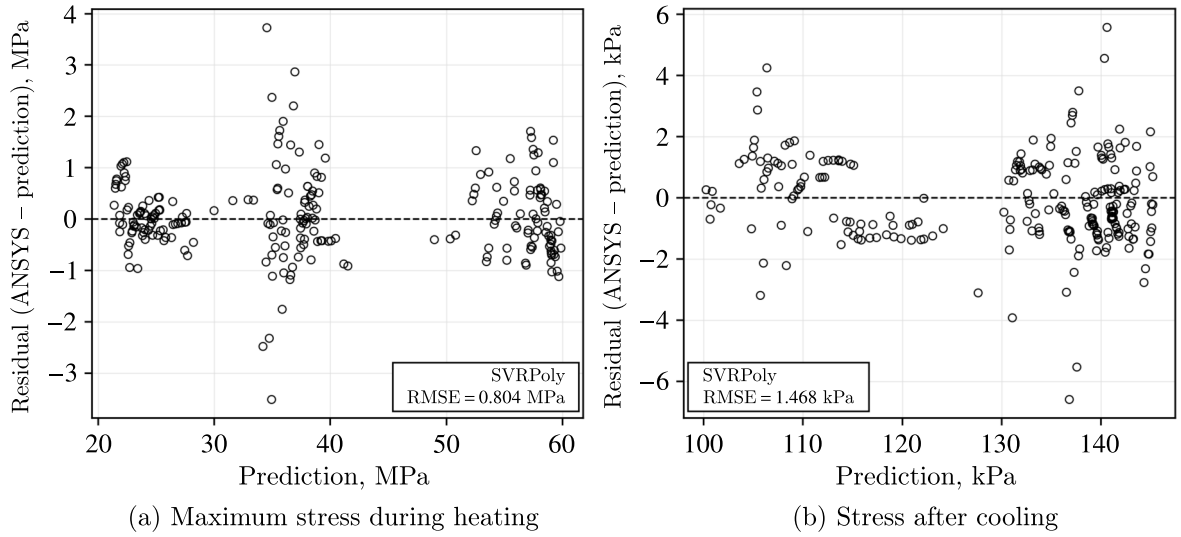
(a) Maximum stress during heating (b) Stress after cooling

Figure 5. Comparison of calculated and predicted stresses on the independent test sample of the unified calculation: (a) maximum equivalent stress during heating ($\sigma_{\max}$, TensorSplineGAM); (b) equivalent stress at the end of cooling (σ_{cool}, TensorSplineGAMLog1p)

A complementary residual diagnostic is shown for polynomial-kernel SVR (SVRPoly) in Fig. 6. Its test RMSE is 0.804 MPa for the maximum heating stress and 1.468 kPa for the stress after cooling, compared with 1.105 MPa for TensorSplineGAM and 1.273 kPa for TensorSplineGAMLog1p, respectively. The models therefore have errors of comparable magnitude. The residuals retain local structure and several larger deviations, particularly for the cooling stress; close overall agreement does not imply uniformly small errors across all regimes.

Evolutionarily synthesized neural-network models

The evolutionary search was performed on the same data split as the calculation of the other models: 711 training, 237 validation, and 237 test regimes. Five independent runs of 20 generations were carried out with a population of 40 individuals and 40 offspring per generation; in total, 4200 candidates were evaluated, all of which completed successfully. NSGA-II selection accounted



(a) Maximum stress during heating (b) Stress after cooling

Figure 6. SVRPoly residuals on the common independent test sample (237 regimes): (a) maximum equivalent stress during heating; (b) equivalent stress after cooling. Each residual is the ANSYS value minus the prediction and is plotted against the prediction. Open circles denote individual regimes; the dashed line marks zero error

for the normalized error of two heating-stage responses, the mean MAPE, and the CPU forward-pass time.

The overall representative selected by the validation criterion was obtained in the third run. Its genome used a common Dense block 64-64-96-128 with ReLU activation, a temperature head of 8 neurons, and a mechanical head of 64 neurons with tanh activation; transfer of the temperature representation to the mechanical branch was not used in the selected architecture. The network contained 33 330 parameters, was trained for 700 epochs, and had a median inference time of 0.239 ms per regime.

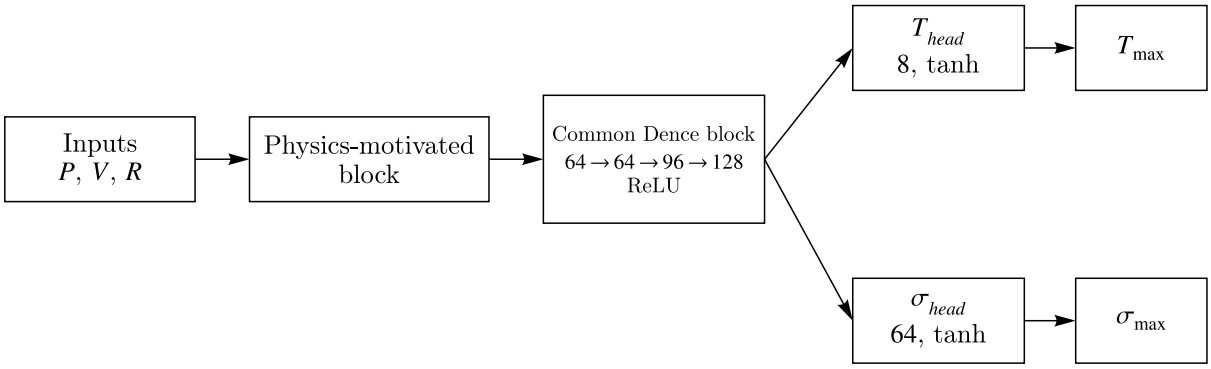


Figure 7. Architecture of the neural network selected by the validation criterion on the common data split. Validation selected representative: run 3.33330 parameters, 700 epochs, 2.239 ms/regime

On the independent test sample, the selected NAS model provided for $T_{\max}$ R^2 = 0.998802, R^2_{adj} = 0.998786, RMSE = 9.816 K, MAE = 4.385 K, MAPE = 0.224 %, and sMAPE = 0.224 %. For $\sigma_{\max}$, the values R^2 = 0.999316, R^2_{adj} = 0.999307, RMSE = 0.354 MPa, MAE = 0.164 MPa, MAPE = 0.433 %, and sMAPE = 0.433 % were obtained. By test RMSE, the best of the five runs for both responses was the fourth, but the representative of the third run is included in the summary table because it was selected without using the test sample.

Table 6 gives a summary comparison of the models selected by the validation criterion; for NAS, rows are given only for $T_{\max}$ and $\sigma_{\max}$, because T_{cool} and σ_{cool} were not predicted in the neural-network experiment.

Table 6. Summary comparison of the best models selected by the validation criterion

Response	Model group	Model	R^2	R^2_{adj}	RMSE	MAE	MAPE, %
$T_{\max}$	Ensemble	Stacking	0.999356	0.999348	7.198 K	4.001 K	0.208
$T_{\max}$	Physics-structured	TS-GAMLog1p	0.992468	0.992371	24.612 K	17.506 K	0.890
$T_{\max}$	NAS	PhysicalNAS, run 3	0.998802	0.998786	9.816 K	4.385 K	0.224
T_{cool}	Ensemble	Stacking	0.999840	0.999838	2.643 K	1.456 K	0.200
T_{cool}	Physics-structured	TS-GAMLog1p	0.997563	0.997532	10.310 K	7.086 K	0.979
$\sigma_{\max}$	Ensemble	Stacking	0.999725	0.999722	0.225 MPa	0.135 MPa	0.375
$\sigma_{\max}$	Physics-structured	TS-GAM	0.993348	0.993262	1.105 MPa	0.735 MPa	1.968
$\sigma_{\max}$	NAS	PhysicalNAS, run 3	0.999316	0.999307	0.354 MPa	0.164 MPa	0.433
σ_{cool}	Ensemble	Stacking	0.998735	0.998719	0.483 kPa	0.219 kPa	0.179
σ_{cool}	Physics-structured	TS-GAMLog1p	0.991199	0.991086	1.273 kPa	0.892 kPa	0.689

Discussion of results

According to the registered metric values, the minimum errors for all four responses among non-NAS models were provided by stacking. For $T_{\max}$, stacking reduced RMSE relative to the selected physics-structured TensorSplineGAMLog1p model by a factor of 3.419 and relative to the selected NAS model by a factor of 1.364. For $\sigma_{\max}$, the corresponding ratios were 4.920 and 1.578. For T_{cool} and σ_{cool}, the neural-network experiment was not performed; for these responses, the comparison was made between stacking and physics-structured models.

The evolutionarily synthesized network quality was between stacking and physics-structured models for the two heating-stage responses.

The physics-structured models have a higher error, but they provide the clearest relation between technological parameters and the predicted quantities. Their advantage lies in the smoothness of the response surface, controlled complexity, and the possibility of analyzing coefficients, derivatives, and pairwise interactions. Therefore, the choice of model is determined by the intended purpose: stacking is appropriate when minimum error is the priority; NAS is appropriate when a two-output approximator of the heating stage is required; and TensorSplineGAM/PhysicalRidge is appropriate when interpretability is the priority.

Permutation importance of the original factors

Permutation importance was evaluated for the fitted models by randomly permuting one original input factor at a time and measuring the increase in RMSE relative to the unpermuted test data. The trained models were kept fixed. Table 7 reports the saved mean RMSE increases for the stacking models selected for the four responses. Importance is expressed in the units of the corresponding response; its magnitude should therefore be compared within each row.

Speed has the highest permutation importance for all four stacking models. The same leading factor is obtained for the selected physics-structured models: permuting speed increases RMSE by 355.675 K for $T_{\max}$, 281.449 K for T_{cool}, 17.927 MPa for $\sigma_{\max}$, and 17.283 kPa for σ_{cool}. Radius ranks second for the temperature responses, whereas power ranks second for the stress responses in

Table 7. Permutation importance for the selected stacking models: mean increase in test RMSE

Response (unit)	Speed V	Radius R	Power P
$T_{\max}$ (K)	378.177	126.164	64.291
T_{cool} (K)	291.861	42.459	23.573
$\sigma_{\max}$ (MPa)	19.008	2.226	2.579
σ_{cool} (kPa)	17.992	4.569	4.707

both groups. These rankings describe the predictive dependence of the fitted surrogates on the original factors within the investigated numerical dataset.

Permutation importance is not an isolated measure of causal physical sensitivity. Its values depend on the fitted model, the sampled factor ranges and combinations, and the calibration embedded in the finite-element data. In particular, source calibration varies between simulated regimes, so the ranking should not be interpreted as the effect of varying speed, while all source-calibration parameters remain fixed. The results do not establish generalization to excluded factor levels or to conditions outside the studied domain. This appendix lists the coefficient vectors and pairwise-interaction matrices of the four selected physics-structured models. Tables A1–A4 describe $T_{\max}$, Tables A5–A8 describe T_{cool}, Tables A9–A12 describe $\sigma_{\max}$, and Tables A13–A16 describe σ_{cool}.

In Tables A1–A16, the coefficients are rounded to 0.001 for compact presentation. For the $T_{\max}$ model: $c = 7.561$, regularization parameter $\alpha = 0.004642$.

Conclusion

Surrogate modeling of the thermomechanical responses of quartz-glass laser polishing was performed using data generated by a previously calibrated finite-element thermoviscoelastic model. The constructed models relate the maximum temperature $T_{\max}$, temperature after cooling T_{cool}, maximum equivalent stress $\sigma_{\max}$, and stress after cooling σ_{cool} to laser power, source travel speed, and laser-spot radius. All model classes were evaluated using the same data split, enabling a consistent comparison of their predictive performance.

The lowest test errors for all four responses were obtained with stacking models combining Random Forest, Gradient Boosting, and XGBoost with RidgeCV as the metamodel. These models achieved $R^2 = 0.998735$–0.999840 and MAPE = 0.179–0.375 %. The corresponding RMSE values were 7.198 K for $T_{\max}$, 2.643 K for T_{cool}, 0.225 MPa for $\sigma_{\max}$, and 0.483 kPa for σ_{cool}. Thus, within the investigated factor domain, ensemble-based surrogate modeling provides highly accurate approximation of the responses generated by the finite-element model.

The physics-structured models produced higher errors than stacking but provided a smooth and interpretable representation of the relationships between laser-processing parameters and thermomechanical responses. TensorSplineGAMLog1p was selected by the validation criterion for $T_{\max}$, T_{cool}, and σ_{cool}, whereas TensorSplineGAM was selected for $\sigma_{\max}$. These models are suitable for response-surface analysis, evaluation of local derivatives and pairwise factor interactions, and physically meaningful interpretation of the energetic, temporal, and geometric characteristics of laser exposure.

Evolutionary neural-architecture search produced a two-output model for simultaneous prediction of $T_{\max}$ and $\sigma_{\max}$. The architecture selected according to the validation criterion achieved $R^2 = 0.998802$ and MAPE = 0.224 % for the maximum temperature and $R^2 = 0.999316$ and MAPE = 0.433 % for the maximum equivalent stress. These results demonstrate the feasibility of automatically synthesizing compact neural approximators of thermomechanical responses while jointly accounting for prediction accuracy, model complexity, and computational cost. Permutation importance analysis showed that the source travel speed is of the greatest importance for the predictive accuracy of the

selected stacking and physics-structured models for all four responses within the investigated numerical dataset; this ranking is not a causal physical sensitivity estimate.

Thus, the results define complementary application domains for the investigated surrogate models. Stacking provides the lowest test error for high-accuracy interpolation within the studied parameter domain; TensorSplineGAM and TensorSplineGAMLog1p provide smooth and physically interpretable representations of the responses; and the evolutionarily synthesized neural network enables simultaneous prediction of thermal and mechanical responses during heating. The resulting surrogate models provide a computational basis for further analysis of multiparametric laser-polishing regimes and for multicriteria optimization with simultaneous consideration of temperature constraints and thermal-stress levels.

Appendix A. Coefficients of the physics-structured models

This appendix lists the coefficient vectors and pairwise-interaction matrices of the four selected physics-structured models. Tables A1–A4 describe $T_{\max}$, Tables A5–A8 describe T_{cool}, Tables A9–A12 describe $\sigma_{\max}$, and Tables A13–A16 describe σ_{cool}.

In Tables A1–A16, the coefficients are rounded to 0.001 for compact presentation. For the $T_{\max}$ model: $c = 7.561$, regularization parameter $\alpha = 0.004642$.

Table A1. Coefficient vectors of the TensorSplineGAMLog1p model for $T_{\max}$

	b0	b1	b2	b3	b4
aR	0.042	0.046	0.003	0.045	−0.032
aP	−0.039	−0.045	−0.040	−0.031	−0.014
aV	0.115	0.115	−0.006	−0.006	−0.110

Table A2. MRP matrix of the TensorSplineGAMLog1p model for $T_{\max}$

i/j	b0	b1	b2	b3	b4
b0	0.013	−0.056	−0.108	−0.055	−0.073
b1	0.027	0.089	0.079	0.038	0.028
b2	−0.079	−0.054	−0.033	−0.031	−0.014
b3	0.019	0.010	0.017	0.019	−0.053
b4	−0.104	−0.085	−0.040	−0.044	0.000

Table A3. MRV matrix of the TensorSplineGAMLog1p model for $T_{\max}$

i/j	b0	b1	b2	b3	b4
b0	0.195	0.195	0.027	0.027	−0.003
b1	0.029	0.029	0.034	0.034	0.128
b2	0.191	0.191	−0.013	−0.013	−0.167
b3	0.055	0.055	0.032	0.032	0.102
b4	0.146	0.146	−0.026	−0.026	−0.258

For the T_{cool} model: $c = 6.488$, $\alpha = 0.021544$.

For the selected TensorSplineGAM model of the maximum equivalent stress during heating $\sigma_{\max}$, the coefficients are given below. The prediction in MPa was specified by the expression $\widehat{\sigma}_{\max} = \max(0, \eta\sigma_{\max})$, where $\eta\sigma_{\max}$ has a tensor-spline form.

The structure of $\eta\sigma_{\max}$ includes additive B-spline components in R, P, V and matrices of pairwise interactions MRP, MRV, and MPV.

Table A4. MPV matrix of the TensorSplineGAMLog1p model for $T_{\max}$

i/j	b0	b1	b2	b3	b4
b0	−0.046	−0.046	−0.094	−0.094	−0.071
b1	−0.011	−0.011	0.002	0.002	−0.184
b2	−0.010	−0.010	−0.021	−0.021	−0.129
b3	−0.021	−0.021	−0.010	−0.010	−0.093
b4	−0.029	−0.029	−0.009	−0.009	−0.026

Table A5. Coefficient vectors of the TensorSplineGAMLog1p model for T_{cool}

	b0	b1	b2	b3	b4
aR	−0.025	−0.059	0.000	0.005	0.017
aP	−0.036	−0.040	−0.035	−0.029	−0.012
aV	0.267	0.267	−0.018	−0.018	−0.251

Table A6. MRP matrix of the TensorSplineGAMLog1p model for T_{cool}

i/j	b0	b1	b2	b3	b4
b0	0.001	−0.047	−0.098	−0.057	−0.075
b1	0.030	0.091	0.077	0.041	0.017
b2	−0.057	−0.041	−0.022	−0.021	−0.008
b3	0.012	0.013	0.005	0.025	−0.068
b4	−0.105	−0.082	−0.038	−0.047	0.005

Table A7. MRV matrix of the TensorSplineGAMLog1p model for T_{cool}

i/j	b0	b1	b2	b3	b4
b0	0.335	0.335	−0.073	−0.073	−0.391
b1	−0.060	−0.060	−0.075	−0.075	−0.108
b2	0.426	0.426	−0.036	−0.036	−0.396
b3	0.034	0.034	−0.010	−0.010	−0.004
b4	0.418	0.418	0.006	0.006	−0.363

Table A8. MPV matrix of the TensorSplineGAMLog1p model for T_{cool}

i/j	b0	b1	b2	b3	b4
b0	−0.078	−0.078	−0.083	−0.083	−0.030
b1	−0.038	−0.038	−0.005	−0.005	−0.127
b2	−0.030	−0.030	−0.021	−0.021	−0.085
b3	−0.040	−0.040	−0.012	−0.012	−0.062
b4	−0.042	−0.042	−0.005	−0.005	−0.006

The intercept $c = 40.738$; regularization parameter $\alpha = 0.000464$. The settings $n_{knots} = 5$, degree = 2, pairwise tensor interactions, and linear extrapolation were used.

For the selected TensorSplineGAMLog1p model of the stress after cooling σ_{cool}, the coefficients are given below. The prediction in KPa was specified by the expression

$$\widehat{\sigma}_{cool} = 10^{-3} \cdot (\exp(\max(0,\ \eta\sigma_{cool})) - 1).$$

The structure of $\eta\sigma_{cool}$ includes additive B-spline components in R, P, V and matrices of pairwise interactions MRP, MRV, and MPV.

The intercept $c = 11.743$; regularization parameter $\alpha = 46.4169$. The settings $n_{knots} = 7$, degree = = 3, pairwise tensor interactions, and linear extrapolation were used.

Table A9. Coefficient vectors of the TensorSplineGAM model for $\sigma_{\max}$

	b0	b1	b2	b3	b4
aR	3.728	1.753	−1.162	1.681	−1.339
aP	−2.625	−2.800	−2.604	−2.077	−1.001
aV	9.550	9.550	0.766	0.766	−10.411

Table A10. MRP matrix of the TensorSplineGAM model for $\sigma_{\max}$

i/j	b0	b1	b2	b3	b4
b0	−8.701	−9.870	−16.412	−10.309	−10.121
b1	−3.664	0.135	−2.485	−3.780	−4.841
b2	−3.190	−1.955	0.416	−0.683	0.268
b3	−0.011	−0.406	−0.318	0.193	−4.421
b4	−4.325	−2.929	0.110	−0.994	1.767

Table A11. MRV matrix of the TensorSplineGAM model for $\sigma_{\max}$

i/j	b0	b1	b2	b3	b4
b0	16.698	16.698	6.405	6.405	−3.956
b1	7.891	7.891	−0.664	−0.664	0.040
b2	16.148	16.148	−1.060	−1.060	−20.148
b3	6.411	6.411	0.739	0.739	−0.281
b4	11.496	11.496	0.467	0.467	−17.920

Table A12. MPV matrix of the TensorSplineGAM model for $\sigma_{\max}$

i/j	b0	b1	b2	b3	b4
b0	−1.921	−1.921	−7.373	−7.373	−4.833
b1	0.259	0.259	−0.640	−0.640	−11.571
b2	0.990	0.990	−2.921	−2.921	−8.313
b3	0.019	0.019	−1.041	−1.041	−7.324
b4	−0.685	−0.685	−1.197	−1.197	−2.582

Table A13. Coefficient vectors of the TensorSplineGAMLog1p model for σ_{cool}

	b0	b1	b2	b3	b4	b5	b6	b7
aR	−0.015	−0.004	−0.001	0.004	0.005	0.005	0.001	−0.004
aP	−0.026	−0.004	−0.010	−0.002	−0.003	0.004	0.004	0.011
aV	0.042	0.010	0.042	0.049	0.012	0.049	−0.091	−0.023

Table A14. MRP matrix of the TensorSplineGAMLog1p model for σ_{cool}

i/j	b0	b1	b2	b3	b4	b5	b6	b7
b0	−0.125	0.061	−0.028	−0.109	−0.040	−0.025	−0.004	0.013
b1	−0.029	0.014	−0.007	−0.027	−0.010	−0.006	−0.001	0.004
b2	0.049	−0.032	0.003	−0.005	−0.011	0.000	0.008	0.022
b3	0.032	−0.039	0.000	0.011	−0.003	0.006	0.013	0.039
b4	−0.071	−0.003	−0.014	0.013	0.008	0.007	0.010	0.039
b5	−0.115	0.008	−0.020	0.019	0.012	0.006	0.011	0.031
b6	−0.116	0.003	−0.026	0.008	0.002	0.010	0.009	0.012
b7	−0.068	−0.012	−0.027	−0.011	−0.013	0.017	0.004	−0.003

Table A15. MRV matrix of the TensorSplineGAMLog1p model for σ_{cool}

i/j	b0	b1	b2	b3	b4	b5	b6	b7
b0	0.401	0.100	0.401	−0.011	−0.003	−0.011	−0.622	−0.155
b1	0.103	0.026	0.103	−0.002	0.000	−0.002	−0.159	−0.040
b2	0.122	0.030	0.122	0.048	0.012	0.048	−0.180	−0.045
b3	0.102	0.026	0.102	0.087	0.022	0.087	−0.142	−0.036
b4	0.058	0.015	0.058	0.086	0.022	0.086	−0.076	−0.019
b5	0.042	0.010	0.042	0.095	0.024	0.095	−0.071	−0.018
b6	0.015	0.004	0.015	0.103	0.026	0.103	−0.107	−0.027
b7	−0.005	−0.001	−0.005	0.105	0.026	0.105	−0.150	−0.038

Table A16. MPV matrix of the TensorSplineGAMLog1p model for σ_{cool}

i/j	b0	b1	b2	b3	b4	b5	b6	b7
b0	0.199	0.050	0.199	0.062	0.016	0.062	−0.800	−0.200
b1	0.078	0.020	0.078	−0.012	−0.003	−0.012	−0.127	−0.032
b2	0.112	0.028	0.112	0.113	0.028	0.113	−0.351	−0.088
b3	0.077	0.019	0.077	0.082	0.020	0.082	−0.200	−0.050
b4	0.079	0.020	0.079	0.041	0.010	0.041	−0.172	−0.043
b5	0.046	0.012	0.046	0.107	0.027	0.107	−0.104	−0.026
b6	0.044	0.011	0.044	0.048	0.012	0.048	−0.028	−0.007
b7	−0.023	−0.006	−0.023	0.125	0.031	0.125	0.081	0.020

References

Abadi M., Barham P., Chen J., Chen Z., Davis A., Dean J., Devin M., Ghemawat S., Irving G., Isard M., Kudlur M., Levenberg J., Monga R., Moore S., Murray D. G., Steiner B., Tucker P., Vasudevan V., Warden P., Wicke M., Yu Y., Zheng X. TensorFlow: A system for large-scale machine learning // 12th USENIX Symposium on Operating Systems Design and Implementation. — 2016. — P. 265–283.

Arbuzov V. I. Osnovy radiatsionnogo opticheskogo materialovedeniya [Fundamentals of radiation optical materials science]. — Saint Petersburg: SPbGU ITMO, 2008. — 284 p. (in Russian).

Breiman L. Random forests // Machine Learning. — 2001. — Vol. 45, No. 1. — P. 5–32. — DOI: 10.1023/A:1010933404324

Chen T., Guestrin C. XGBoost: A scalable tree boosting system // Proceedings of the 22nd ACM SIGKDD International Conference on Knowledge Discovery and Data Mining. — 2016. — P. 785–794. — DOI: 10.1145/2939672.2939785

Deb K., Pratap A., Agarwal S., Meyarivan T. A fast and elitist multiobjective genetic algorithm: NSGA-II // IEEE Transactions on Evolutionary Computation. — 2002. — Vol. 6, No. 2. — P. 182–197. — DOI: 10.1109/4235.996017

Dong G., Wong J. C., Lestandi L., Mikula J., Vastola G., Jhon M. H., Dao M. H., Kizhakkinan U., Ford C. S., Rosen D. W. A part-scale, feature-based surrogate model for residual stresses in the laser powder bed fusion process // Journal of Materials Processing Technology. — 2022. — Vol. 304. — Art. 117541. — DOI: 10.1016/j.jmatprotec.2022.117541

Efron B., Tibshirani R. J. An introduction to the bootstrap. — New York: Chapman & Hall, 1993. — 456 p.

Eilers P. H. C., Marx B. D. Flexible smoothing with B-splines and penalties // Statistical Science. — 1996. — Vol. 11, No. 2. — P. 89–121. — DOI: 10.1214/ss/1038425655

Elsken T., Metzen J. H., Hutter F. Neural architecture search: A survey // Journal of Machine Learning Research. — 2019. — Vol. 20, No. 55. — P. 1–21.

Emelyanov V. A., Shershnev E. B., Nikityuk Yu. V., Sokolov S. I., Aushev I. Yu. Optimizatsiya lazernoy polirovki kvartsevogo stekla s ispol'zovaniem metoda planirovaniya vychislitel'nykh eksperimentov [Optimization of laser polishing of quartz glass using the method of planning computational experiments] // Problemy fiziki, matematiki i tekhniki [Problems of Physics, Mathematics and Technics]. — 2022. — No. 2 (51). — P. 26–30 (in Russian). — DOI: 10.54341/20778708_2022_2_51_26

Forrester A. I. J., Keane A. J. Recent advances in surrogate-based optimization // Progress in Aerospace Sciences. — 2009. — Vol. 45, No. 1–3. — P. 50–79. — DOI: 10.1016/j.paerosci.2008.11.001

Friedman J. H. Greedy function approximation: A gradient boosting machine // The Annals of Statistics. — 2001. — Vol. 29, No. 5. — P. 1189–1232. — DOI: 10.1214/aos/1013203451

He T., Wei C., Jiang Z., Zhao Y., Shao J. Super-smooth surface demonstration and the physical mechanism of CO_2 laser polishing of fused silica // Optics Letters. — 2018. — Vol. 43, No. 23. — P. 5777–5780. — DOI: 10.1364/OL.43.005777

Hemmasian A. P., Ogoke F., Akbari P., Malen J., Beuth J., Barati Farimani A. Surrogate modeling of melt pool temperature field using deep learning // Additive Manufacturing Letters. — 2023. — Vol. 5. — Art. 100123. — DOI: 10.1016/j.addlet.2023.100123

Hildebrand J., Hecht K., Bliedtner J., Müller H. Advanced analysis of laser beam polishing of quartz glass surfaces // Physics Procedia. — 2012. — Vol. 39. — P. 277–285. — DOI: 10.1016/j.phpro.2012.10.039

Hildebrand J., Hecht K., Bliedtner J., Müller H. Laser beam polishing of quartz glass surfaces // Physics Procedia. — 2011. — Vol. 12. — P. 452–461. — DOI: 10.1016/j.phpro.2011.03.056

Hoerl A. E., Kennard R. W. Ridge regression: Biased estimation for nonorthogonal problems // Technometrics. — 1970. — Vol. 12, No. 1. — P. 55–67. — DOI: 10.1080/00401706.1970.10488634

Jiang P., Zhou Q., Shao X. Surrogate model-based engineering design and optimization. — Singapore: Springer, 2020. — 240 p. — DOI: 10.1007/978-981-15-0731-1

Karniadakis G. E., Kevrekidis I. G., Lu L., Perdikaris P., Wang S., Yang L. Physics-informed machine learning // Nature Reviews Physics. — 2021. — Vol. 3. — P. 422–440. — DOI: 10.1038/s42254-021-00314-5

Li X., Polydorides N. Time-efficient surrogate models of thermal modeling in laser powder bed fusion // Additive Manufacturing. — 2022. — Vol. 59. — Art. 103122. — DOI: 10.1016/j.addma.2022.103122

Lu G., Li X., Wang D., Wang K. Process parameter optimization for CO_2 laser polishing of fused silica using the Taguchi method // Materials. — 2024. — Vol. 17, No. 3. — Art. 709. — DOI: 10.3390/ma17030709

Menold T., Onuseit V., Buser M., Haas M., Bär N., Michalowski A. Laser material processing optimization using Bayesian optimization: A generic tool // Light: Advanced Manufacturing. — 2024. — Vol. 5. — Art. 32. — DOI: 10.37188/lam.2024.032

Mohajerani S., Bordatchev E. V., Tutunea-Fatan O. R. Recent developments in modeling of laser polishing of metallic materials // Lasers in Manufacturing and Materials Processing. — 2018. — Vol. 5. — P. 395–429. — DOI: 10.1007/s40516-018-0071-5

Nikitjuk Yu. V., Prokhorenko V. A., Marchanka L. N. Software Package for surrogate modeling of laser polishing processes of quartz glass: computer program. — Copyright holder: Francisk Skorina Gomel State University. — Application filed on October 5, 2026; registration pending.

Nikityuk Yu. V., Marchenko L. N., Serdyukov A. N., Bruttan Iu. V. Simulation of laser polishing for fused quartz // Computer Research and Modeling. — 2026. — Vol. 18, No. 2. — P. 399–421. — DOI: 10.20537/2076-7633-2026-18-2-399-421

Nikityuk Yu. V., Prokhorenko V. A., Kulyba A. I. Mnogokriterial'naya optimizatsiya parametrov lazernoy rezki kvartsevogo stekla s primeneniem neyrosetevogo modelirovaniya i geneticheskogo algoritma [Multicriteria optimization of quartz glass laser cutting parameters using neural-network modeling

and a genetic algorithm] // Problemy fiziki, matematiki i tekhniki [Problems of Physics, Mathematics and Technics]. — 2023. — No. 3 (56). — P. 26–31 (in Russian). — DOI: 10.54341/20778708_2023_3_56_26

Nikityuk Yu. V., Vasil'ev A. F., Marchenko L. N., Ma J., Wang L., Qin Y., Aushev I. Yu. Opredelenie parametrov upravlyaemogo lazernogo raskalyvaniya silikatnykh stekol s ispol'zovaniem regressionnykh, neyrosetevykh i nechetkikh modeley [Determination of parameters for controlled laser cleaving of silicate glasses using regression, neural-network and fuzzy models] // Problemy fiziki, matematiki i tekhniki [Problems of Physics, Mathematics and Technics]. — 2024. — No. 2 (59). — P. 32–38 (in Russian). — DOI: 10.54341/20778708_2024_2_59_32

Nisar S. Optimization of laser beam geometry for controlling thermal stresses in CO_2 laser glass cutting // Lasers in Manufacturing and Materials Processing. — 2025. — Vol. 12, No. 2. — P. 298–317. — DOI: 10.1007/s40516-025-00289-6

Nowak K. M., Baker H. J., Hall D. R. Efficient laser polishing of silica micro-optic components // Applied Optics. — 2006. — Vol. 45, No. 1. — P. 162–171. — DOI: 10.1364/AO.45.000162

Pedregosa F., Varoquaux G., Gramfort A., Michel V., Thirion B., Grisel O., Blondel M., Prettenhofer P., Weiss R., Dubourg V., Vanderplas J., Passos A., Cournapeau D., Brucher M., Perrot M., Duchesnay É. Scikit-learn: Machine learning in Python // Journal of Machine Learning Research. — 2011. — Vol. 12. — P. 2825–2830.

Queipo N. V., Haftka R. T., Shyy W., Goel T., Vaidyanathan R., Kevin Tucker P. Surrogate-based analysis and optimization // Progress in Aerospace Sciences. — 2005. — Vol. 41, No. 1. — P. 1–28. — DOI: 10.1016/j.paerosci.2005.02.001

Raissi M., Perdikaris P., Karniadakis G. E. Physics-informed neural networks: A deep learning framework for solving forward and inverse problems involving nonlinear partial differential equations // Journal of Computational Physics. — 2019. — Vol. 378. — P. 686–707. — DOI: 10.1016/j.jcp.2018.10.045

Rosa B., Hascoet J.-Y., Mognol P. Modeling and optimization of laser polishing process // Applied Mechanics and Materials. — 2014. — Vol. 575. — P. 766–770. — DOI: 10.4028/www.scientific.net/AMM.575.766

Sacks J., Welch W. J., Mitchell T. J., Wynn H. P. Design and analysis of computer experiments // Statistical Science. — 1989. — Vol. 4, No. 4. — P. 409–423. — DOI: 10.1214/ss/1177012413

Seabold S., Perktold J. Statsmodels: Econometric and statistical modeling with Python // Proceedings of the 9th Python in Science Conference. — 2010. — P. 92–96. — DOI: 10.25080/Majora-92bf1922-011

Shershnev E. B., Nikityuk Yu. V., Sokolov S. I., Shershnev A. E. Issledovanie protsessa lazernoy polirovki kvartsevogo stekla [Investigation of the process of laser polishing of quartz glass] // Problemy fiziki, matematiki i tekhniki [Problems of Physics, Mathematics and Technics]. — 2015. — No. 4 (25). — P. 45–49 (in Russian).

Simpson T. W., Peplinski J. D., Koch P. N., Allen J. K. Metamodels for computer-based engineering design: Survey and recommendations // Engineering with Computers. — 2001. — Vol. 17, No. 2. — P. 129–150. — DOI: 10.1007/PL00007198

Smola A. J., Schölkopf B. A tutorial on support vector regression // Statistics and Computing. — 2004. — Vol. 14. — P. 199–222. — DOI: 10.1023/B:STCO.0000035301.49549.88

Solheid J. S., Elkaseer A., Wunsch T., Scholz S., Seifert H. J., Pfleging W. Multiobjective optimization of laser polishing of additively manufactured Ti-6Al-4V parts for minimum surface roughness and heat-affected zone // Materials. — 2022. — Vol. 15, No. 9. — Art. 3323. — DOI: 10.3390/ma15093323

Stanley K. O., Miikkulainen R. Evolving neural networks through augmenting topologies // Evolutionary Computation. — 2002. — Vol. 10, No. 2. — P. 99–127.

Sysoev V. K. Laser etching and polishing of quartz tubes // Glass and Ceramics. — 2003. — Vol. 60, No. 7–8. — P. 223–226.

Tibshirani R. Regression shrinkage and selection via the Lasso // Journal of the Royal Statistical Society: Series B. — 1996. — Vol. 58, No. 1. — P. 267–288.

Virtanen P., Gommers R., Oliphant T. E. et al. SciPy 1.0: Fundamental algorithms for scientific computing in Python // Nature Methods. — 2020. — Vol. 17. — P. 261–272. — DOI: 10.1038/s41592-019-0686-2

Wolpert D. H. Stacked generalization // Neural Networks. — 1992. — Vol. 5, No. 2. — P. 241–259. — DOI: 10.1016/S0893-6080(05)80023-1

Zou H., Hastie T. Regularization and variable selection via the elastic net // Journal of the Royal Statistical Society: Series B. — 2005. — Vol. 67, No. 2. — P. 301–320. — DOI: 10.1111/j.1467-9868.2005.00503.x